Doping-controlled quantum magnetization plateau and high-field ferroelectricity in multiferroic $Ni_{2-x}T_xV_2O_7$ (T = Zn or Mn)

T. Li,[1] H. W. Wang,[1,2,*] Y. R. Song,[1] C. Dong,[1] R. Chen,[3] M. Yang,[1] and J. F. Wang[1]

[1]*Wuhan National High Magnetic Field Center and School of Physics, Huazhong University of Science and Technology, Wuhan 430074, China*

[2]*Department of Applied Physics, School of Science, Wuhan University of Science and Technology, Wuhan 430081, China*

[3]*College of Physics and Electronic Engineering, Xinyang Normal University, Xinyang 464000, China*

(Received 8 August 2023; revised 4 October 2023; accepted 17 November 2023; published 11 December 2023)

The synchronized observation of a quantum magnetization plateau and multiferroicity is of particular interest in frustrated antiferromagnets, but the modulation of two different fascinating phenomena is greatly challenging and urgently desired. Here, we report an efficient approach with chemical substitutions to achieve flexible control of a half quantum magnetization plateau and high-field ferroelectricity in the $S = 1$ skew-chain antiferromagnet $Ni_2V_2O_7$. In Zn-doped cases, the half quantum magnetization plateau is remarkably broadened with an increasing concentration on dopants, such as a giant variation reaching 69.3% at $x = 0.7$, suggesting the existence of a larger spin gap than before. In contrast, the width of magnetization plateaus for Mn-doped samples pronouncedly shrinks about -37.4% at $x = 0.2$, and then tends to stabilization upon further increasing x. Intriguingly, we find that the end of half magnetization plateaus locates in the same position between two groups of samples. In particular, the nontrivial magnetoelectric coupling related with the high-field ferroelectricity performs an identical evolution for $Ni_{2-x}T_xV_2O_7$ (T = Zn or Mn) by sweeping magnetic fields. As a consequence, a close correlation between the half magnetization plateau and ferroelectricity is confirmed, indicating that the high-field polarization is derived from peculiar magnetic moments in $Ni_2V_2O_7$. Possible origins for the Zn- and Mn-doping effects on the quantum magnetization plateau and multiferroicity are discussed. In addition, high-field phase diagrams with the plateau and ferroelectricity are constructed for these doped compounds. Therefore, these experimental findings open an additional avenue to tune the quantum magnetization plateau and magnetically induced ferroelectricity, simultaneously.

DOI: 10.1103/PhysRevB.108.224414

I. INTRODUCTION

The simultaneous appearance of quantum magnetization plateaus and magnetically induced ferroelectricities in a frustrated antiferromagnet sheds light on the study of exotic quantum states. These materials, such as $CuFeO_2$ [1–3] and $Ni_3V_2O_8$ [4–6], have a peculiar requirement for magnetic structures and display a complex magnetic phase diagram, so they have attracted considerable interest in the physics community. Recently, we reported that both the half magnetization plateau and the ferroelectricity occur simultaneously in the $S = 1$ skew-chain compound $Ni_2V_2O_7$ [7,8], which possesses an ellipsoidal cycloidal incommensurate magnetic structure at low temperatures [9]. Under high magnetic fields, its magnetization process results from competing exchange interactions among Ni ions described using a dimer+monomer model proposed by Cao *et al.* [10]. However, more experimental investigations of the coupling and tunability with the half magnetization plateau and ferroelectricity need to be made.

The family of vanadate oxides with a general formula $R_2V_2O_7$ (R = Mn, Co, Ni, and Cu) is highly sensitive to external perturbations including not only pressures [11], and magnetic/electric fields [7,8,10,12–14], but also chemical substitutions [15–18]. For $Cu_2V_2O_7$, three different polymorphs have been verified, namely, the α (orthorhombic), β (monoclinic), and γ (triclinic) phases [19]. Intriguingly, a polymorphic transition from the α- to β-$Cu_2V_2O_7$ can be driven by a moderate substitution of nonmagnetic Zn ions at the Cu site, which in turn causes a pronounced influence on magnetic properties [17,18]. The compound $Mn_2V_2O_7$ crystallizes in a quasi-two-dimensional distorted honeycomb lattice with two different structural phases α (triclinic) and β (monoclinic) [20]. As the temperature decreases, a reversible first-order structural transition from the monoclinic phase to the triclinic phase emerges around T_s, accompanied with the paraelastic to ferroelastic ordering transition [16,21]. Importantly, T_s can be tuned by the partial substitution of Ni, Co, and Ca ions at Mn sites. In detail, T_s moves to higher temperatures for the Ni and Co doping, but Ca doping leads to a completely opposite trend in $Mn_2V_2O_7$ [16]. It seems that chemical substitutions on A sites are an efficient means to modulate the physical property of $R_2V_2O_7$. However, until now, there has been little evidence that both $Ni_2V_2O_7$ and $Co_2V_2O_7$ are tuned by chemical substitutions despite the fact that the half magnetization plateau and ferroelectricity are simultaneously observed in two compounds by sweeping magnetic fields [7,8,13].

As a typical representative of the $R_2V_2O_7$ family, $Ni_2V_2O_7$ is considered as a skew-chain antiferromagnet [22].

*Corresponding author: wanghaowen1@hust.edu.cn

Structurally, it comprises the nonmagnetic ion V^{5+} ($3d^0$, $S = 0$) and magnetic ions Ni^{2+} ($3d^8$, $S = 1$), which are located in two different sites (Ni1 and Ni2). The alternative arrangement of edge-shared $Ni1O_6$ and $Ni2O_6$ octahedra forms the skew chain along the c direction, and adjacent chains are separated by corner-shared nonmagnetic tetrahedra VO_4. Magnetically, $Ni_2V_2O_7$ behaves as a classical three-dimensional (3D) antiferromagnet with long-range ordering below 7 K and demonstrates a field-driven spin-flop transition at low magnetic fields. According to the measurement of ultrahigh magnetic fields, the wide 1/2- and 3/4-like magnetization plateaus are observed in fields of 11.7–34.8 T and 55.6–87.0 T, respectively [7,8,10]. Compared with $Co_2V_2O_7$, the half quantum magnetization plateau is broader and the phase diagram looks richer in $Ni_2V_2O_7$ [7,8,13]. In addition, the flat 3/4-like plateau is merely stabilized in the latter under ultrahigh magnetic fields [10]. In ferroelectric aspects, two magnetically induced ferroelectric phases are observed below and above half magnetization plateaus [7]. Hence, $Ni_2V_2O_7$ could serve as a good candidate to modulate the quantum magnetization plateau and ferroelectricity by chemical doping.

In this work, we report results of the doped study on polycrystalline samples of $Ni_{2-x}T_xV_2O_7$ (T = Zn or Mn, $0 \leqslant x \leqslant 0.7$) in the high magnetic field up to 58 T. Detailed characterizations, involving crystal structure, specific heat, magnetic susceptibility, low-/high-field magnetization, and high-field ferroelectric polarization measurements, are carried out for all samples. The half quantum magnetization plateau reveals an absolutely opposite evolution between Zn- and Mn-doped samples, i.e., the width and height of plateaus. Note that the end of half magnetization plateaus is stabilized in the same position between two groups of samples. In addition, it is found that the end of the plateaus is almost synchronous with the onset of high-field ferroelectric phases for all samples, suggesting high-field ferroelectricity from peculiar spins in $Ni_2V_2O_7$. Finally, high-field phase diagrams with the plateau and ferroelectricity are established for these doped compounds.

II. EXPERIMENT DETAILS

A series of $Ni_{2-x}T_xV_2O_7$ (T = Zn or Mn, $0 \leqslant x \leqslant 0.7$) polycrystalline samples were prepared by conventional solid-state reaction methods as in the previous report [7]. In detail, stoichiometric amounts of high-purity NiO, V_2O_5, and ZnO or MnO powders were ground thoroughly and then calcined in air at 500 °C-700 °C for 36 h each with several intermediate grinding sequences. Finally, the resultant powder was pressed into pellets and subsequently sintered in air at 600 °C for 72 h. The crystal structure of as-grown samples was characterized using powder x-ray diffraction (XRD, Philips X'Pert PRO) with Cu $K\alpha$ radiation ($\lambda = 1.5406$ Å) at room temperature. The doping content x and elemental mappings were characterized using a combination of a Shimadzu 8050G field emission electron probe microanalyzer (EPMA) and an Oxford energy dispersive x-ray spectrometer (EDS).

Magnetization (M) measurements, including both magnetic field H and temperature T dependences, were performed using a Quantum Design superconducting quantum interference device (SQUID). For $\chi(T)$ curves, the applied magnetic field was stabilized at $H = 0.1$ T. After the zero-field cooling sequence, the $M(H)$ data were detected at $T = 2$ K for all samples. Specific heat data were collected by a Quantum Design physical properties measurement system (PPMS). The pulsed high-field $M(H)$ at $T = 1.6$ K was measured by the standard induction method using a coaxial pickup coil and calibrated employing a comparison with the low-field magnetic curve. Gold electrodes were deposited on parallel surfaces of the rectangular sample and an electric field E was perpendicularly applied to the golden surface. High-field ferroelectric polarizations (P) were obtained by the pyroelectric technique at various temperatures, that was derived from integrating the pyroelectric current with the time. Note that a bias field of $E = +800$ kV/m was used before and preserved during the short pulse to completely polarize ferroelectric (FE) domains in the samples. The pulsed high field with a 10.5-ms short-pulse wave was generated by a nondestructive magnet in the Wuhan National High Magnetic Field Center. It is worth mentioning that we study polycrystalline samples rather than single crystals owing to the limit of ionic doping concentrations in single crystal $Ni_2V_2O_7$. In addition, the polycrystalline sample with a large size is beneficial to the measurement of electric polarizations in high magnetic fields.

III. RESULTS AND DISCUSSION

A. Structural characterization and chemical homogeneity

The quality of as-grown samples is determined by the collected XRD spectra. All samples are single phased with a monoclinic crystalline structure ($P2_1/c$), as presented in Fig. S1 of the Supplemental Material [23]. In comparison with $Cu_{2-x}Zn_xV_2O_7$, no structural phase transition is observed; even the dopant Zn or Mn substitutes Ni with the doping concentration up to $x = 0.7$. To get details on the evolution of lattice parameters, the Rietveld refinement of XRD data is carried out for all Zn- or Mn-doped $Ni_2V_2O_7$ samples, and the refined results with $x = 0.3$ are depicted in Figs. 1(a) and 1(b) as a typical example. The discrepancy between the refined and measured patterns is tiny with all reliability factors R_{wp} below 3.09%. For other samples, their values are stabilized in similar levels (see Figs. S2 and S3 of the Supplemental Material [23]). Derived unit cell parameters of the $Ni_2V_2O_7$ are $a = 6.5207$, $b = 8.2989$, $c = 9.3645$, and $\beta = 99.8898°$, which are in good agreement with earlier reports from powder neutron scattering [9]. The obtained structural factors, such as a, b, c, β, cell volume V, and c/b ratio dependent Zn or Mn content x are shown in Figs. 1(c)–1(h), respectively. With increasing x, lattice constants for two groups of samples, i.e., a, b, c, β, monotonously increase in a qualitative sense. It is indicated that the ionic radius (r) of Zn and Mn ions is larger than that of the $Ni^{2+}(3d^8)$ ion, according to the empirical Vegard's law. Importantly, the variation of lattice constants is more striking in Mn-doped samples; e.g., the expansion of the a axis for $Ni_{1.3}Mn_{0.7}V_2O_7$ ($\sim 1.26\%$) is much larger than that of $Ni_{1.3}Zn_{0.7}V_2O_7$ ($\sim 0.54\%$). Consequently, for all possible oxidation states of the Mn ion, it is most likely that the high-spin ($S = 5/2$) state of the Mn^{2+} ($3d^5$) ion substitutes the Ni^{2+} ion in $Ni_2V_2O_7$ since only its size is larger than

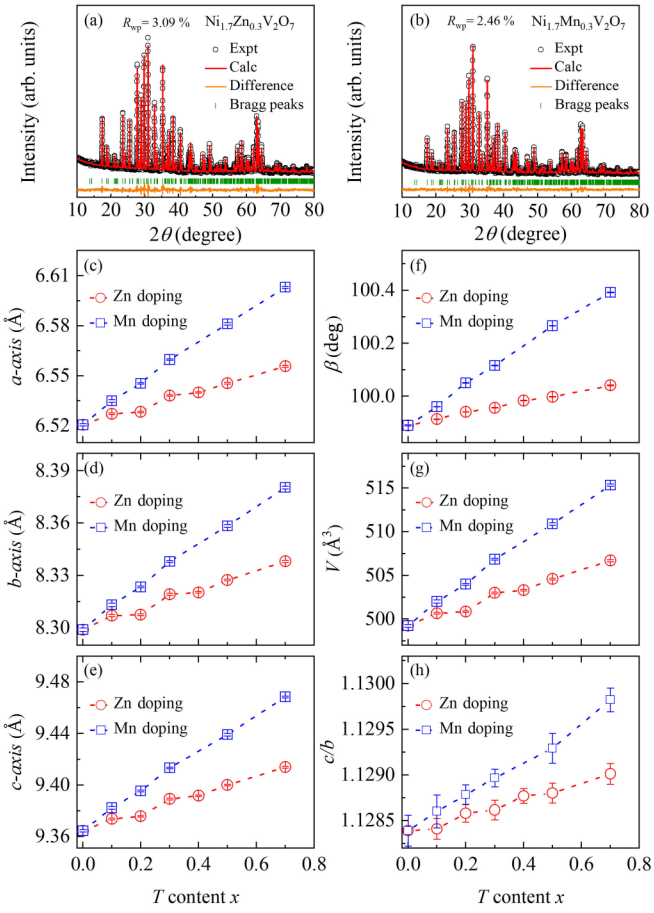

FIG. 1. Rietveld refinement of the XRD spectra for (a) $Ni_{1.7}Zn_{0.3}V_2O_7$ and (b) $Ni_{1.7}Mn_{0.3}V_2O_7$ at room temperature. Evaluated lattice factors: (c) a, (d) b, (e) c, (f) β, (g) cell volume V, and (h) c/b ratio for the $Ni_{2-x}Zn_xV_2O_7$ (red dots) and $Ni_{2-x}Mn_xV_2O_7$ (blue squares).

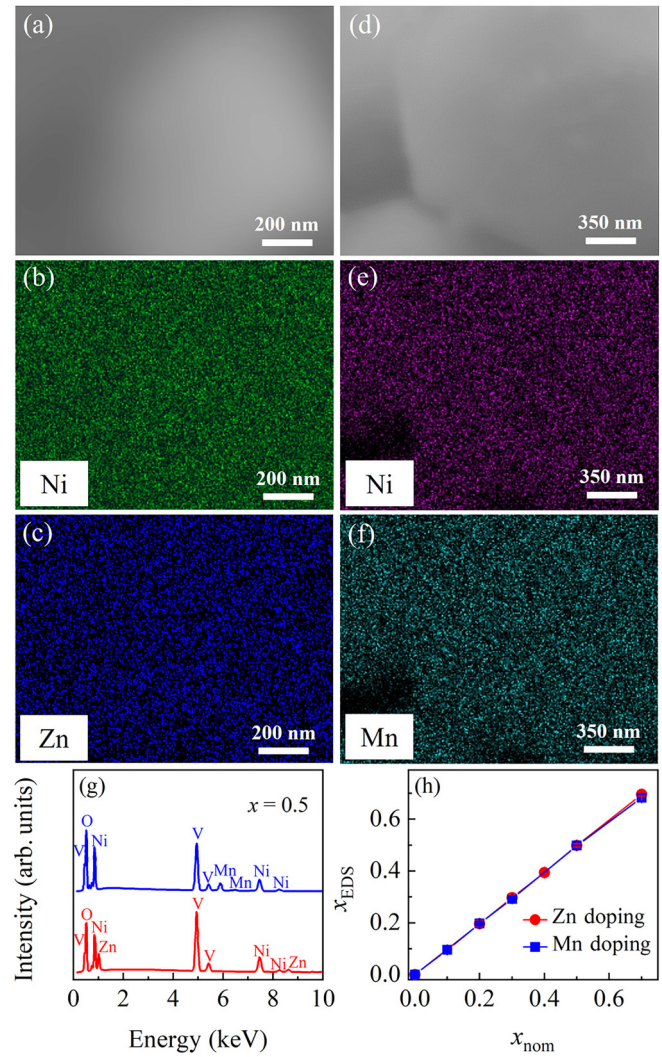

FIG. 2. The SEM image for (a) $Ni_{1.5}Zn_{0.5}V_2O_7$, and corresponding elemental mappings of (b) Ni and (c) Zn. The SEM image for (d) $Ni_{1.5}Mn_{0.5}V_2O_7$, and corresponding elemental mappings of (e) Ni and (f) Mn. (g) The typical EDS spectra of the samples with $x = 0.5$. (h) Measured dopant content x_{EDS} as a function of the nominal value x_{nom}.

the ionic radius of Zn^{2+} ($3d^{10}$) ions; i.e., $r(Ni^{2+}) = 0.69$ Å $< r(Zn^{2+}) = 0.74$ Å $< r(Mn^{2+}) = 0.83$ Å [24]. As reported by earlier works, lattice parameters play a quite crucial role in magnetic behaviors of $Ni_2V_2O_7$ due to linking the superexchange paths [8,10], as evidenced hereafter.

Diffraction experiments are complemented by EDS measurements, which can examine elemental distributions and compositions of the sample. All crystals are confirmed to be homogeneous and stoichiometric without observing any aggregation of ions, according to EDS results shown in Fig. 2 and Tables S3–S5 of the Supplemental Material [23]. Here, we take $x = 0.5$ as an example and exhibit the EDS mappings in Figs. 2(a)–2(f). The zinc or manganese element is homogeneously distributed in the system, and they are indeed doped into $Ni_2V_2O_7$ and substituted for nickel (see Table S3 of the Supplemental Material [23]). It is worth noting that there is no contrast between grains and grain boundaries. In addition, as observed in Fig. 2(h), the results suggest that the measured content x_{EDS} is almost identical with the nominal value x_{nom} for all samples, and its standard deviation is illustrated in detail in the Tables S4 and S5 of the Supplemental Material [23]. In the present work, the x concentration refers to x_{nom} unless stated elsewhere.

B. Temperature dependent magnetic phase transitions

Figures 3(a) and 3(b) show the temperature dependence of the magnetic susceptibility χ for $Ni_{2-x}Zn_xV_2O_7$ and $Ni_{2-x}Mn_xV_2O_7$ measured at 0.1 T, respectively. For the undoped $Ni_2V_2O_7$, it undergoes two continuous magnetic phase transitions at a low temperature of $T_{N1} = 7.0$ K and $T_{N2} = 6.0$ K, identified by moderate peaks in the $\chi(T)$ curves, which are well consistent with earlier works [7,8]. Native transitions at T_{N1} and T_{N2} are also clearly manifested in specific-heat data with single crystals, indicating the onset of antiferromagnetic orderings with Ni2 ions and the appearance of ellipsoidal cycloidal incommensurate magnetic structures for Ni1 and Ni2 spins, respectively [9]. By introducing Zn ions into the Ni site, these transitions monotonically move toward the low temperature. More details of the variation of magnetic transitions upon Zn doping are presented in the inset of Fig. 3(a). Both T_{N1} and T_{N2} display little shift for $x \leqslant 0.1$, while these sharply

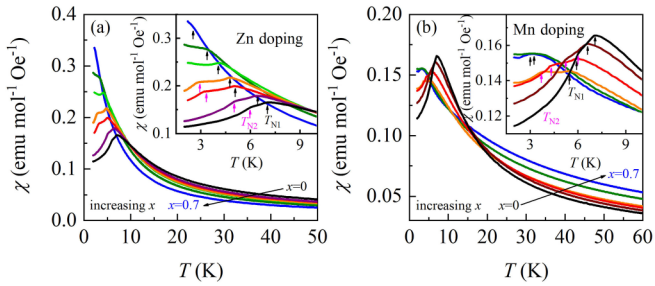

FIG. 3. Temperature dependence of the magnetic susceptibility χ for (a) $Ni_{2-x}Zn_xV_2O_7$ and (b) $Ni_{2-x}Mn_xV_2O_7$ samples with $x = 0$, 0.1, 0.2, 0.3, 0.4, 0.5, 0.7. The inset shows the amplified curve at low temperature.

decrease from $x = 0.1$ to 0.2, and then gradually decrease for $x > 0.2$. Finally, T_{N1} becomes vague at $x = 0.7$ which is visible in the temperature derivative $d\chi/dT$, and T_{N2} disappears at $x > 0.3$. Furthermore, the χ in magnitude becomes markedly stronger with increasing x at low temperature. With the corporation of Mn ions, the transition temperature with T_{N1} and T_{N2} slowly decreases and the χ is persistently suppressed in the range $0 \leqslant x \leqslant 0.3$ [see the inset of Fig. 3(b)]. Further increasing x gives rise to a sharp reduction in T_{N1} and leads to a complete disappearance of T_{N2}, but a cusp related to antiferromagnetic (AFM) orderings is clearly observed even up to $x = 0.7$. Meanwhile, all samples with $x \geqslant 0.5$ show a moderate enhancement in magnetism, namely, the measured χ first weakens and then strengthens as the Mn ion concentration increases. Interestingly, in the high-temperature region, the sample with Mn substitutions gets stronger in magnetic behaviors while the magnetism becomes weaker with the Zn ion doping (see black arrows). This suggests that the different dopant in $Ni_2V_2O_7$ has an influence on not only magnetic phase transitions but also its magnetism.

The evolution of both T_{N1} and T_{N2} with ion substitutions in $Ni_2V_2O_7$ can be further supported by the specific heat measurements. Figure 4(a) exhibits the temperature dependence of the specific heat C for $Ni_{2-x}Zn_xV_2O_7$ at zero applied magnetic field. The $C(T)$ curve of the undoped sample clearly depicts two λ-like peaks at around 6.8 and 5.9 K, basically corresponding to the $\chi(T)$ data seen in Fig. 3. As expected, both peaks gradually shift to the lower temperature with increasing x. Similarly, the peak at T_{N2} is invisible at $x > 0.3$ and a weak hump is identified at T_{N1} as the Zn ion content further increases, suggesting the complete suppression of the spiral spin ordered (SSO) feature. Based on the comprehensive measurement of $\chi(T)$ and $C(T)$ curves, a temperature–Zn content (T-x) phase diagram with $Ni_{2-x}Zn_xV_2O_7$ is well demonstrated in Fig. 4(b). Three distinct regions are well separated in the diagram, which are defined as the PM, PO, and SSO phases, respectively. According to the previous study, the low- and high-field ferroelectric phases can be confirmed below and above half magnetization plateaus, respectively [7]. Namely, the light blue area represents the low-field FE phase, which can be tuned by changing the Zn content x and T. This suggests that the low-field FE phase should result from a noncollinear spin configuration in $Ni_2V_2O_7$. In addition, these transition points of T_{N1} and T_{N2} derived from $C(T)$ curves are

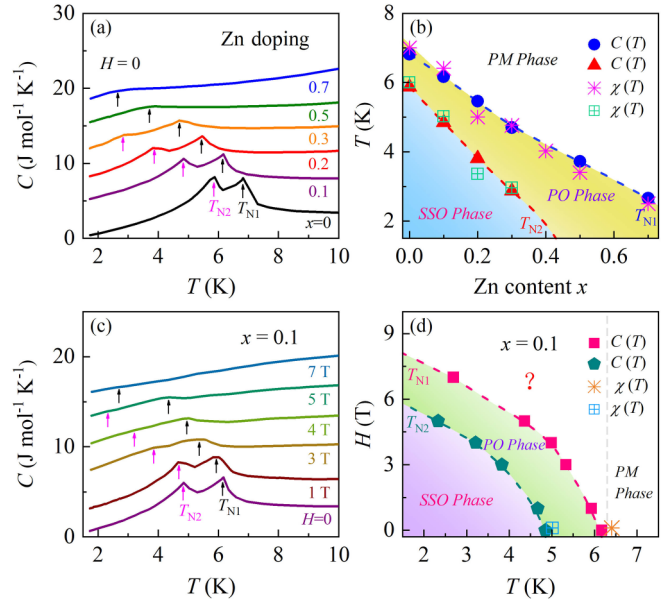

FIG. 4. (a) Temperature dependence of the specific heat for the Zn-doped cases. (b) Temperature-dopant concentration (T-x) phase diagram based on $C(T)$ and $\chi(T)$ data with the Zn doping. (c) Temperature dependence of the specific heat for $Ni_{1.9}Zn_{0.1}V_2O_7$ at different magnetic fields. (d) Field-temperature (H-T) phase diagram based on the collected data of $C(T)$ and $\chi(T)$ with the $Ni_{1.9}Zn_{0.1}V_2O_7$ sample. For clarity, $C(T)$ curves have been offset vertically. The above diagrams are constituted by paramagnetic (PM), partially ordered (PO), and spiral spin ordered (SSO) phases.

well consistent with that of $\chi(T)$ curves. As a consequence, for polycrystalline samples with the Mn substitution at the Ni site, the T-x phase diagram is proposed only relying on the $\chi(T)$ curve in Fig. S5 in the Supplemental Material [23]. Compared with the Zn doping, the SSO phase of the Mn doping is sustained up to $x = 0.7$, which may be ascribed to unique magnetic interactions due to magnetic dopants. To get more information about the development of T_{N1} and T_{N2}, the $C(T)$ for $x = 0.1$ of the Zn doping is measured in various applied magnetic fields of 0–7 T, as demonstrated in Fig. 4(c). As the H increases, T_{N1} moves to lower temperatures, which is generally observed in samples with AFM orderings. Moreover, the amplitude of this peak is drastically reduced due to the redistribution of magnetic entropy. Eventually, it becomes vague at $H = 7$ T, suggesting the complete suppression of AFM orderings and the appearance of unusual spin configurations in high fields. On the other hand, the peak at T_{N2} also moves toward lower temperatures with an increase of H, and finally is wiped out above 5 T. The variation of both T_{N1} and T_{N2} with H are summarized in the magnetic field–temperature (H-T) phase diagram of $Ni_{1.9}Zn_{0.1}V_2O_7$, as depicted in Fig. 4(d). For all other samples, it is similar to the development of the H-T diagram. It is worth mentioning that high-field measurements reveal the 1/2- and 3/4-like magnetization plateau in $Ni_2V_2O_7$, accompanied by a high-field FE phase between them. Therefore, the phase transition with multiferroic properties in doped samples is very desirable and inspires us to explore under the high magnetic field.

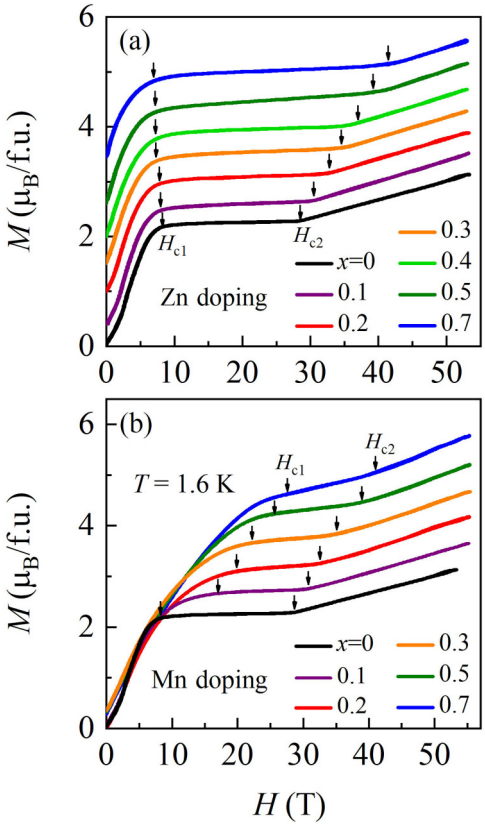

FIG. 5. High-field $M(H)$ curves at $T = 1.6$ K for (a) $Ni_{2-x}Zn_xV_2O_7$ and (b) $Ni_{2-x}Mn_xV_2O_7$ samples. For a better version, the curves in (a), (b) have been shifted vertically, and the well-defined magnetization plateau between H_{c1} and H_{c2} is presented clearly.

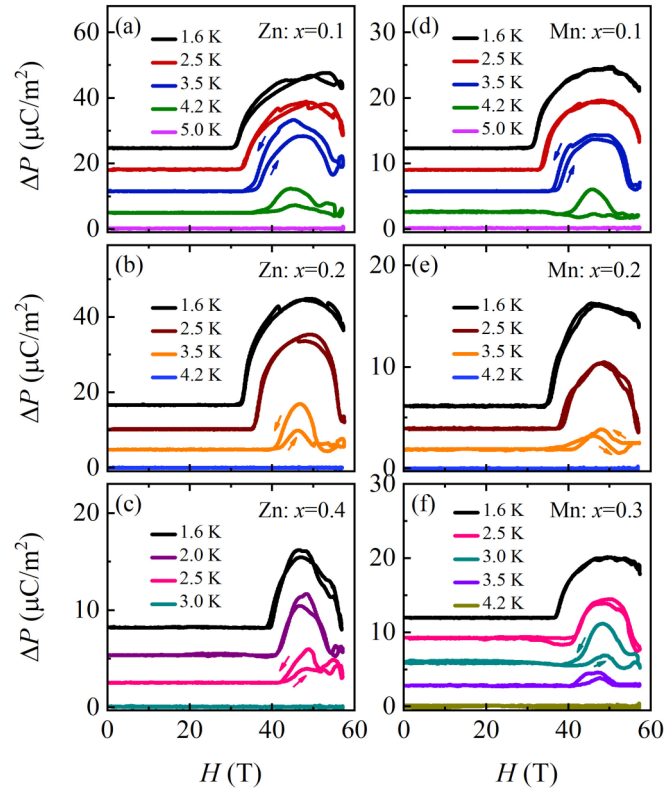

FIG. 6. ΔP as a function of H measured at various temperatures under the magnetic field up to 58 T. For the Zn doping: (a) $x = 0.1$, (b) $x = 0.2$, and (c) $x = 0.4$; Mn doping: (d) $x = 0.1$, (e) $x = 0.2$, and (f) $x = 0.3$. The arrows denote the field-rising (-falling) sweeps. Prior to measurements, the sample is cooled down to target temperatures under a poling electric field of $+800$ kV/m, and then maintained during the short pulse to completely polarize ferroelectric domains. For clarity, the curves have been moved vertically.

C. Magnetic field induced quantum magnetization plateau

Figure 5 exhibits the H dependence of magnetizations of the $Ni_{2-x}Zn_xV_2O_7$ [Fig. 5(a)] and $Ni_{2-x}Mn_xV_2O_7$ [Fig. 5(b)] samples in pulsed magnetic fields up to 53 and 55 T, respectively. In addition to the low-field spin-flop transition H_{sf}, a well-defined half magnetization plateau between $H_{c1} = 8.3$ T and $H_{c2} = 28.7$ T with a width of 20.4 T ($\Delta H = H_{c2}$-H_{c1}) is clearly observed in the undoped compound $Ni_2V_2O_7$, very close to the result of a single crystal [8]. Further increasing the magnetic field, the magnetization increases linearly with H up to 53 T. For the Zn-doped sample, the doping leads to a slight decrease for H_{c1}, whereas H_{c2} moves to the higher H significantly. For instance, H_{c1} is reduced by approximately -1.3 T while H_{c2} is enhanced by approximately 12.8 T as x is up to 0.7. As a result, the width of the magnetization plateau ΔH becomes broader due to the Zn doping (see Fig. S6(a) of the Supplemental Material [23]). Differently, the transition H_{c1} dramatically increases from 8.3 T at $x = 0$ to 17.0 T at $x = 0.1$, and then gradually shifts toward a higher H upon further Mn doping. However, the variation of H_{c2} is nearly identical between Zn- and Mn-doped samples. Hence, the width of the half magnetization plateau for the latter begins to diminish markedly and then undergoes a tiny change, eventually presenting a stable value, as shown in Fig. S6(a) of the Supplemental Material [23]. Furthermore, as the Mn doping rises, this plateau gradually becomes less clear and has a positive slope, but two transitions with H_{c1} and H_{c2} can still be identified even in the $x = 0.7$ sample. Note that the intensity of the measured magnetization derived from $M(H)$ demonstrates an opposite trend above H_{c1}; i.e., the Zn doping leads to a continuous suppression of magnetic orders while the Mn-doped cases enhance magnetic orders, as plotted in Fig. S6(b) of the Supplemental Material [23].

D. High-field ferroelectric states and the phase diagrams

We further study the ferroelectric polarization P changes of the Zn- and Mn-doped $Ni_2V_2O_7$ samples in pulsed magnetic fields up to 58 T, in which the variation of P is indicated by the $\Delta P = P(H)$-$P(H = 0)$, and typical data are demonstrated in Fig. 6. For all samples, the magnitude value of ΔP is almost maintained at zero below 30 T. These observations are reminiscent of the FE properties of the parent compound for a comparison, that two magnetically induced FE phases are stabilized in the low-field region of 0–5 T (LF-FE) and the high-field region above 29 T (HF-FE) at 1.7 K [7]. The disappearance of the LF-FE phase is possibly attributed to the substituted effect or it may exist but the tiny P is beyond the sensitive limit of our equipment. We then focus on the

HF-FE of the different Zn-doping content x, where it starts at a critical field of H_{cri1}, as shown in Figs. 6(a)–6(c). Increasing x gives rise to a discernible enhancement in H_{cri1} at 1.6 K; e.g., it shifts from $H_{cri1} \sim 30.8$ T at $x = 0.1$ to $H_{cri1} \sim 38.3$ T at $x = 0.4$. However, the maximum intensity of ΔP sharply decreases from 23.1 μC/m^2 at $x = 0.1$ to 7.9 μC/m^2 at $x = 0.4$, suggesting a strong suppression of the ferroelectricity due to Zn substitutions. As H is further increased, ΔP displays a sudden fall and even the sample with $x = 0.4$ reenters the paraelectric state at a higher field of $H_{cri2} \sim 56.7$ T at the lowest temperatures. On the other hand, for the sample with $x = 0.1$ exhibited in Fig. 6(a), P is completely suppressed to zero above 4.2 K. As the Zn-doping level further increases, the disappearance of the HF-FE takes place at a lower temperature, such as $x = 0.2$ above 3.5 K and $x = 0.4$ above 2.5 K. In comparison with Zn-doped cases, Figures 6(d)–6(f) show the polarization behavior with the incorporation of Mn results. Several obvious features from the $\Delta P(H)$ curve are clearly seen. First, only the HF-FE is observed by the application of high magnetic fields. Second, at the same temperature, H_{cri1} moves toward the high-field side with increasing Mn doping. Meanwhile, the maximum intensity of ΔP above H_{cri1} gradually decreases. Third, the critical temperature of the fully suppressed HF-FE with $\Delta P = 0$ drops from 5.0 K at $x = 0.1$ to 4.2 K at $x = 0.3$. As a consequence, despite magnetization measurements having exhibited distinctly different behaviors between $Ni_{2-x}Zn_xV_2O_7$ and $Ni_{2-x}Mn_xV_2O_7$, the evolution of ferroelectric properties with different dopants presents many similar features.

Summarizing our experimental data on the high-field measurement of magnetizations and electric polarizations, both magnetic field–dopant concentration (H-x) and magnetic field–temperature (H-T) are proposed for $Ni_{2-x}T_xV_2O_7$ (T = Zn or Mn), as demonstrated in Figs. 7(a), and 7(b) and 7(c), respectively. The evolution of the half quantum magnetization plateau is denoted as colored areas between H_{c1} and H_{c2}, which are derived from high-field magnetizations data. From Fig. 7(a) it can be directly observed that the incorporation of Zn ions leads to a substantial extension of the field range of the half plateau. In contrast, it sharply starts to shrink and then remains around a constant in Mn-doped $Ni_2V_2O_7$ samples. Note that the above interesting phenomena mostly result from the different H_{c1} because of the identical change of the H_{c2} with two groups of samples. Furthermore, the critical point H_{cri1} derived from the $P(H)$ curves is in good agreement with H_{c2}, suggesting an intrinsic coupling between the magnetism and ferroelectricity in the high-field region. Namely, the HF-EF state in $Ni_{2-x}T_xV_2O_7$ is driven by their magnetic orderings. On the other hand, the HF-EF can be tuned effectively by varying the dopant content x and temperature T. Compared with the nondoped sample, the region of electric polarizations gradually decreases as the doping concentration x increases. Importantly, a similar tendency in the development of the HF-EF is well identified between the Zn and Mn doping, as shown in Figs. 7(b) and 7(c).

E. Possible origin for the Zn- and Mn-doping effects

Our experimental results have demonstrated a tuned quantum magnetization plateau by chemical doping in the vanadate

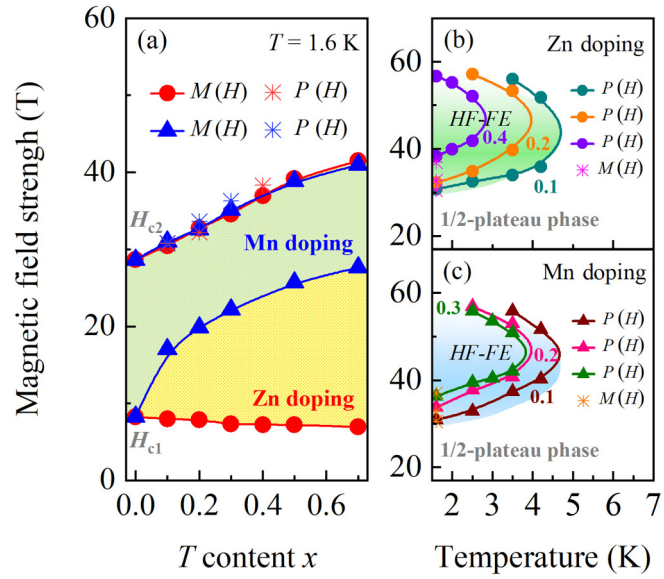

FIG. 7. (a) Field-dopant concentration (H-x) phase diagram is summarized for $Ni_{2-x}Zn_xV_2O_7$ and $Ni_{2-x}Mn_xV_2O_7$ samples, based on the result of high-field magnetizations (solid dots and triangles) and electric polarizations (stars). The yellow (light blue) area represents the half quantum magnetization plateau for Zn- (Mn-) doped cases. Field-temperature (H-T) phase diagram based on the collected high-field data of $P(H)$ and $M(H)$ for (b) Zn- and (c) Mn-doping samples, where HF-FE denotes the high-field ferroelectric phase. Shaded regions represent the ferroelectric phase of the nondoped sample $Ni_2V_2O_7$, which is obtained from Ref. [7].

compound $Ni_{2-x}T_xV_2O_7$ (T = Zn or Mn). Particularly, the width and height of half magnetization plateaus in $Ni_2V_2O_7$ show a completely opposite evolution between the dopant Zn and Mn ions. However, the magnetic field for the onset and end of the high-field ferroelectricity is almost identified with each other. In the following, we will discuss the possible origin of the observed phenomenon resulting from chemical substitutions. As aforementioned, the width of the half quantum magnetization plateaus is generally defined as $\Delta H = H_{c2}$-H_{c1}, where H_{c1} (H_{c2}) represents the onset (end) of plateaus. A recent study on magnetization processes around H_{c1} is given by Cao *et al.*; i.e., the H_{c1} is unstable and intensively depends on field sweep rates and temperatures [10]. Subsequently, Hase *et al.* considered that half magnetization plateaus are mainly attributed to the weakly coupled Ni2 monomers in $Ni_2V_2O_7$ by the neutron diffraction technique [9]. Namely, it is possible that chemical substitutions can effectively control the critical field of half quantum magnetic plateaus. To better understand the different influence for the H_{c1} between $Ni_{2-x}Zn_xV_2O_7$ and $Ni_{2-x}Mn_xV_2O_7$, the isothermal magnetization $M(H)$ is performed in the low field with increasing x, as exhibited in Fig. 8. As expected, the $M(H)$ curve of the $Ni_2V_2O_7$ polycrystalline sample displays a roughly linear increase below 1.0 T because of its AFM ground state. As H increases, a jump at $H_{sf} = 2.7$ T is identified by a closer look and well established by the sharp dM/dH peak, indicating a field-induced spin-flop transition. It is not rare and often occurs at transition metal oxides with alternative AFM orders, such as Sr_2IrO_4 [25]. With further increasing

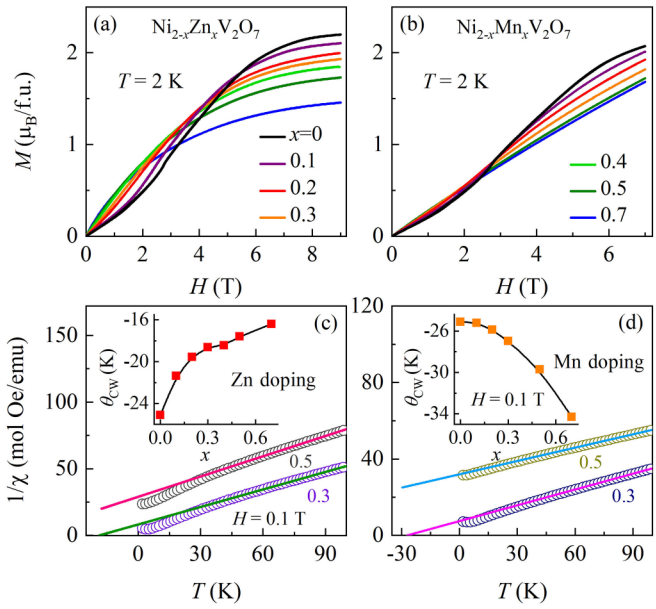

FIG. 8. Measured magnetization as a function of magnetic fields at $T = 2$ K for (a) $Ni_{2-x}Zn_xV_2O_7$ and (b) $Ni_{2-x}Mn_xV_2O_7$ samples. Representative results with Curie-Weiss fittings for the (c) Zn and (d) Mn doping, where the open dot denotes the experimental data and the thin line denotes the result of fittings. The inset shows the Zn or Mn concentration x dependence of the Curie-Weiss temperature θ_{CW}, respectively.

H, the $M(H)$ curve smoothly increases and slowly tends to a fake saturation above 8.0 T, which is a well-defined half magnetization plateau and has been undoubtedly evidenced by previous reports [7]. In Zn-doped cases, the H_{c1} moves slightly toward the low magnetic field with increasing doping levels, suggesting a reduced AFM interaction between Ni2-Ni2 ions. It is well established that the H_{sf} is gradually moved down from 2.7 T at $x = 0$ to 1.7 T at $x = 0.2$ and disappears above 0.3, as shown in Fig. 8(a). In addition, upon Zn ion doping, the profile of the $M(H)$ curve increasingly becomes the paraboliclike pattern which is the type characteristic of paramagnetism [26,27]. As direct evidence, the Curie-Weiss temperature θ_{CW} is obviously enlarged with increasing x, such as from $\theta_{CW} = -25.1$ K at $x = 0$ to $\theta_{CW} = -16.4$ K at $x = 0.7$ [see the inset of Fig. 8(c)]. On the contrary, the Mn dopant gives rise to a more linear $M(H)$ curve at low fields [Fig. 8(b)], suggesting the stronger antiferromagnetic coupling generated among classical Ni2 ions [28,29]. Correspondingly, the Curie-Weiss temperature θ_{CW} gradually diminishes from approximately -25.1 K at $x = 0$ to -34.3 K at $x = 0.7$, as presented in the inset of Fig. 8(d). It is worth mentioning that the average field sweep rate and temperature are identical for all $M(H)$ curves to confirm the intrinsic variation of H_{c1} from dopants.

On the other hand, based on the dimer+monomer model proposed by Gao *et al.*, three nearest-neighbor (NN) exchange interactions expressed as J_1, J_2, and J_3 exist in the spin Heisenberg model of $Ni_2V_2O_7$, wherein the NN interchain J_3 leads to strongly AFM coupled Ni1 dimers with a large spin gap (Δ-J_3) [8,10]. The critical field for the end of half plateaus, H_{c2}, could represent one closed gap among these quantized states. Analogous to the AFM trimer compound $SrMn_3P_4O_{14}$ [30], the half quantum magnetization plateau is a paramagnetic ground state in $Ni_2V_2O_7$, and there is an energy difference lying in the ground and excited state. If the Zeeman energy from magnetic fields is greater than the energy difference, half magnetic plateaus are finished and followed by a quantum phase transition. It has been established that lattice parameters play a quite crucial role in these exchange interactions of the $Ni_2V_2O_7$ due to linking the superexchange paths [8,10]. According to theory calculations, the NN interchain interaction J_3 has an opposite tendency with the distance between Ni1-Ni1 in dimers. We plot in Fig. 1 the structural factors dependent on Zn and Mn content x. The lattice parameters, including a, b, and c values, show a significant variation; e.g., a (b) is much enhanced by approximately 1.26% (0.98%) for Mn doping as x is up to 0.7, as shown in Figs. 1(c) and 1(d), respectively. As expected, such pronounced expansion of lattice parameters would weaken the interaction J_3. Accordingly, the spin gap gradually gets larger as the Zn- or Mn-doping level increases, and the higher magnetic field is required in order to observe the end of half quantum magnetization plateaus in $Ni_2V_2O_7$ (see Fig. 5). In addition, the varied height of the half magnetization plateaus in $Ni_2V_2O_7$ is determined by the magnetism of the dopants; e.g., the amplitude of the plateaus is lower (higher) than that of the parent compound for nonmagnetic Zn ions (magnetic Mn ions). In short, the combined variation of both H_{c1} and H_{c2} generates a controllable width of half quantum magnetization plateaus by chemical doping.

Note that the Zn or Mn substituting for Ni in $Ni_2V_2O_7$ is expected to only lead to the changed crystal structures rather than introduce itinerant carriers due to the equal valance states between Ni^{2+} and Zn^{2+} (Mn^{2+}) ions. In theory, the doping with itinerant carriers can effectively tune the position of magnetization plateaus by strict analytical and numerical calculations [31,32]. In particular, the doping within a high range of carrier concentrations has the ability to simultaneously reduce the height and critical field of plateaus [31]. Apparently, this mechanism does not fit the current experimental phenomenon. Here, the control of quantum magnetization plateaus, which is studied mainly focusing on the growth of new magnetic materials [33–35] and the acquirement of higher field strengths [10,36–38], has been experimentally realized utilizing chemical substitutions.

On the subject of ferroelectricities, Chen *et al.* have shown that two ferroelectric phases are located below and above half magnetic plateaus in $Ni_2V_2O_7$ [7]. Intriguingly, the low-field ferroelectricity disappears for all doped samples in our studies. Very recently, the magnetic structure of $Ni_2V_2O_7$ has been confirmed below T_{N2} by powder neutron diffraction experiments; it is an ellipsoidal cycloidal incommensurate magnetic structure with both Ni1 and Ni2 in the *ab* plane [9]. Consequently, a possible reason is that the field-induced spin flop is significantly weakened due to the reduced magnetocrystalline anisotropy by chemical doping, further breaking the spiral spin orders [see Figs. 8(a) and 8(b)]. Macroscopically, the amplitude of low-field ferroelectric polarizations becomes weak and even vanishes exceeding the measured resolution of the equipment. With regard to the high-field ferroelectricity, it is certain that ferroelectric phases derive from peculiar magnetic

moments since the end of half plateaus corresponds to the onset of ferroelectric phases in all samples. However, it is still a puzzle that the microscopic mechanism of the magnetically driven ferroelectricity belongs to the spin current mechanism or exchange-striction mechanism. Further investigations on spin systems are necessary for the $Ni_2V_2O_7$ under high magnetic fields.

IV. CONCLUSION

In summary, we demonstrate a systematic comparison on the lattice parameter, specific heat, magnetic susceptibility, magnetization, and ferroelectric polarization between Zn- and Mn-doped $Ni_2V_2O_7$ samples. As the doping level gradually increases, lattice constants for two groups of samples monotonously expand in qualitative senses, indicating that the ionic radius of the dopants is larger than that of the Ni^{2+} ion, i.e., Zn^{2+} and Mn^{2+}. Magnetically, the flexible control of the half quantum magnetization plateau in $Ni_2V_2O_7$ is realized utilizing chemical substitutions rather than itinerant carriers. Furthermore, the variation trend with magnetization plateaus is completely opposite for the Zn and Mn doping. On the other hand, the onset of high-field ferroelectric phases moves toward higher magnetic field with increasing doping, for both Zn and Mn ions. In particular, we find a close relation between the magnetism and high-field ferroelectricity, implying high-field polarizations from magnetic moments in $Ni_2V_2O_7$. Additionally, high-field phase diagrams with the plateau and ferroelectricity are constructed for these doped compounds. These works thus provide some insight on the tunability of the quantum magnetization plateau and high-field ferroelectricity in multiferroics.

ACKNOWLEDGMENTS

This work was supported by the National Natural Science Foundation of China (Grants No. 12104351, No. 12074135, and No. 12104388), the Hubei Province Natural Science Foundation of China (Grant No. 2021CFB027), and the China Postdoctoral Science Foundation (Grant No. 2023M731209).

[1] F. Wang and A. Vishwanath, Spin phonon induced collinear order and magnetization plateaus in triangular and kagome antiferromagnets: Applications to $CuFeO_2$, Phys. Rev. Lett. **100**, 077201 (2008).

[2] T. Lummen, C. Strohm, H. Rakoto, and P. Van Loosdrecht, Mapping the magnetic phase diagram of the frustrated metamagnet $CuFeO_2$, Phys. Rev. B **81**, 224420 (2010).

[3] H. Tamatsukuri, S. Mitsuda, T. Nakajima, K. Shibata, C. Kaneko, K. Takehana, Y. Imanaka, N. Terada, H. Kitazawa, and K. Prokes, Activation of frozen ferroelectric domain wall by magnetic field sweeping in multiferroic $CuFeO_2$, Phys. Rev. B **93**, 174101 (2016).

[4] G. Lawes, A. B. Harris, T. Kimura, N. Rogado, R. J. Cava, A. Aharony, O. Entin-Wohlman, T. Yildirim, M. Kenzelmann, C. Broholm, and A. P. Ramirez, Magnetically driven ferroelectric order in $Ni_3V_2O_8$, Phys. Rev. Lett. **95**, 087205 (2005).

[5] J. Wang, M. Tokunaga, Z. Z. He, J. I. Yamaura, A. Matsuo, and K. Kindo, High magnetic field induced phases and half-magnetization plateau in the $S = 1$ kagome compound $Ni_3V_2O_8$, Phys. Rev. B **84**, 220407(R) (2011).

[6] Y. Liu, J. Wang, Z. He, C. Lu, Z. Xia, Z. Ouyang, C. Liu, R. Chen, A. Matsuo, Y. Kohama, K. Kindo, and M. Tokunaga, Unusual magnetoelectric memory and polarization reversal in the kagome staircase compound $Ni_3V_2O_8$, Phys. Rev. B **97**, 174429 (2018).

[7] R. Chen, J. Wang, Z. Ouyang, Z. He, S. Wang, L. Lin, J. Liu, C. Lu, Y. Liu, C. Dong, C. Liu, Z. Xia, A. Matsuo, Y. Kohama, and K. Kindo, Magnetic field induced ferroelectricity and half magnetization plateau in polycrystalline $R_2V_2O_7$ (R = Ni, Co), Phys. Rev. B **98**, 184404 (2018).

[8] Z. Ouyang, Y. Sun, J. Wang, X. Yue, R. Chen, Z. Wang, Z. He, Z. Xia, Y. Liu, and G. Rao, Novel half-magnetization plateau and nematiclike transition in the $S = 1$ skew chain $Ni_2V_2O_7$, Phys. Rev. B **97**, 144406 (2018).

[9] M. Hase, A. Dönni, N. Terada, V. Y. Pomjakushin, J. R. Hester, K. C. Rule, and Y. Matsuo, Neutron diffraction studies under zero and finite magnetic fields of the 1/2 quantum magnetization plateau compound $Ni_2V_2O_7$, Phys. Rev. B **107**, 224415 (2023).

[10] J. Cao, Z. Ouyang, X. Liu, T. Xiao, Y. Song, J. Wang, Y. Ishii, X. Zhou, and Y. Matsuda, Unusual dimerization and magnetization plateaus in $S = 1$ skew chain $Ni_2V_2O_7$ observed at 120 T, Phys. Rev. B **106**, 184409 (2022).

[11] H. Wu, D. Hsieh, T. Yen, P. Sun, D. C. Kakarla, J. Her, Y. Matsuda, C. Chang, Y. Lai, M. Gooch, L. Deng, K. Webber, C. Lee, M. Chou, C. Chu, and H. Yang, Pressure and magnetic field effects on ferroelastic and antiferromagnetic orderings in honeycomb-lattice $Mn_2V_2O_7$, Phys. Rev. B **102**, 075130 (2020).

[12] R. Chen, J. F. Wang, Z. W. Ouyang, M. Tokunaga, A. Y. Luo, L. Lin, J. M. Liu, Y. Xiao, A. Miyake, Y. Kohama, C. L. Lu, M. Yang, Z. C. Xia, K. Kindo, and L. Li, Successive electric-polarization switches in the $S = 1/2$ skew chain $Co_2V_2O_7$ induced by a high magnetic field, Phys. Rev. B **100**, 140403(R) (2019).

[13] L. Yin, Z. Ouyang, J. Wang, X. Yue, R. Chen, Z. He, Z. Wang, Z. Xia, and Y. Liu, Anisotropic magnetization plateaus in $S_{\text{eff}} = 1/2$ skew-chain single-crystal $Co_2V_2O_7$, Phys. Rev. B **99**, 134434 (2019).

[14] G. Gitgeatpong, M. Suewattana, S. Zhang, A. Miyake, M. Tokunaga, P. Chanlert, N. Kurita, H. Tanaka, T. J. Sato, Y. Zhao, and K. Matan, High-field magnetization and magnetic phase diagram of α-$Cu_2V_2O_7$, Phys. Rev. B **95**, 245119 (2017).

[15] G. Gitgeatpong, Y. Zhao, J. Fernandez-Baca, T. Hong, T. Sato, P. Piyawongwatthana, K. Nawa, P. Saeaun, and K. Matan, Magnetic structure and spin dynamics of the quasi-two-dimensional antiferromagnet Zn-doped copper pyrovanadate, Phys. Rev. B **106**, 214438 (2022).

[16] H. Chen, C. Yeh, T. Kuo, D. C. Kakarla, H. Wu, T. Yen, S. Huang, H. Chou, M. Chou, H. Chen, S. Kuo, Y. Chuang, C. Chang, U. Eckstein, N. khansur, K. Webber, and H. Yang, Unique multiferroics with tunable ferroelastic transition in antiferromagnet $Mn_2V_2O_7$, Mater. Today Phys. **23**, 100623 (2022).

[17] J. Pommer, V. Kataev, K.-Y. Choi, P. Lemmens, A. Ionescu, Y. Pashkevich, A. Freimuth, and G. Güntherodt, Interplay between structure and magnetism in the spin-chain compound (Cu, Zn)$_2$V$_2$O$_7$, Phys. Rev. B **67**, 214410 (2003).

[18] B. Chattopadhyay, M. A. Ahmed, S. Bandyopadhyay, R. Singha, and P. Mandal, Magnetic ordering induced ferroelectricity in α-Cu$_2$V$_2$O$_7$ studied through non-magnetic Zn doping, J. Appl. Phys. **121**, 094103 (2017).

[19] S. Bhowal, J. Sannigrahi, S. Majumdar, and I. Dasgupta, A comparative study of electronic, structural, and magnetic properties of α-, β-, and γ-Cu$_2$V$_2$O$_7$, Phys. Rev. B **95**, 075110 (2017).

[20] J. Sannigrahi, D. Adroja, R. Perry, M. Gutmann, V. Petricek, and D. Khalyavin, Commensurate to incommensurate magnetic phase transition in honeycomb-lattice pyrovanadate Mn$_2$V$_2$O$_7$, Phys. Rev. Mater. **3**, 113401 (2019).

[21] L.-D. Chen, L.-H. Shu, G. Liu, P. Nie, Y. Shao, Y.-C. Luo, Y.-Y. Lv, H.-M. Lu, Z.-W. Zhu, X.-X. Xi, J. Zhou, F.-Z. Huang, Z.-X. Cheng, S.-H. Yao, Y. Chen, and Y.-F. Chen, Magnetic field tuning of magnetic-and structure-phase transition in Mn$_2$V$_2$O$_7$ crystals, J. Phys. Chem. C **126**, 5055 (2022).

[22] Z. He, J.-I. Yamaura, Y. Ueda, and W. Cheng, Crystal growth and multiple magnetic transitions of the spin-1 chain system Ni$_2$V$_2$O$_7$, Phys. Rev. B **79**, 092404 (2009).

[23] See Supplemental Material at http://link.aps.org/supplemental/10.1103/PhysRevB.108.224414 for more experimental results: powder x-ray diffraction patterns and details of Rietveld refinement parameters for all samples; EDS results of all samples; scanning electron microscopy (SEM) image and corresponding elemental mappings of Ni, Zn (Mn), V, O for $x = 0.5$; temperature-dopant concentration (T-x) phase diagram for Ni$_{2-x}$Mn$_x$V$_2$O$_7$ ($0 \leqslant x \leqslant 0.7$); estimated width of the magnetization plateau ΔH and derived value of magnetizations at different magnetic fields; details of Curie-Weiss fittings for all samples.

[24] R. D. Shannon, Revised effective ionic radii and systematic studies of interatomic distances in halides and chalcogenides, Acta Crystallogr., Sect. A **32**, 751 (1976).

[25] H. Wang, C. Lu, J. Chen, Y. Liu, S. Yuan, S.-W. Cheong, S. Dong, and J.-M. Liu, Giant anisotropic magnetoresistance and nonvolatile memory in canted antiferromagnet Sr$_2$IrO$_4$, Nat. Commun. **10**, 2280 (2019).

[26] A. Ney, T. Kammermeier, K. Ollefs, S. Ye, V. Ney, T. C. Kaspar, S. A. Chambers, F. Wilhelm, and A. Rogalev, Anisotropic paramagnetism of Co-doped ZnO epitaxial films, Phys. Rev. B **81**, 054420 (2010).

[27] R. Nair, M. Sepioni, I.-L. Tsai, O. Lehtinen, J. Keinonen, A. V. Krasheninnikov, T. Thomson, A. Geim, and I. Grigorieva, Spin-half paramagnetism in graphene induced by point defects, Nat. Phys. **8**, 199 (2012).

[28] Y. Chang, J. Wang, W. Wang, C. Liu, B. You, M. Liu, S. Zheng, M. Shi, C. Lu, and J.-M. Liu, Linear magnetoelectric memory and training effect in the honeycomb antiferromagnet Co$_4$Nb$_2$O$_9$, Phys. Rev. B **107**, 014412 (2023).

[29] Y. Tang, J. Zhang, L. Lin, R. Chen, J. Wang, S. Zheng, C. Li, Y. Zhang, G. Zhou, L. Huang, Z. Yan, X. Lu, D. Wu, X. Huang, X. Jiang, and J.-M. Liu, Metamagnetic transitions and magnetoelectricity in the spin-1 honeycomb antiferromagnet Ni$_2$Mo$_3$O$_8$, Phys. Rev. B **103**, 014112 (2021).

[30] M. Hase, V. Y. Pomjakushin, A. Dönni, T. Yang, R. Cong, and J. Lin, Direct observation of the ground state of a 1/3 quantum magnetization plateau in SrMn$_3$P$_4$O$_{14}$ using neutron diffraction measurements, J. Phys. Soc. Jpn. **83**, 104701 (2014).

[31] C. A. Lamas, S. Capponi, and P. Pujol, Combined analytical and numerical approach to study magnetization plateaux in doped quasi-one-dimensional antiferromagnets, Phys. Rev. B **84**, 115125 (2011).

[32] G. Roux, S. White, S. Capponi, and D. Poilblanc, Zeeman effect in superconducting two-leg ladders: Irrational magnetization plateaus and exceeding the Pauli limit, Phys. Rev. Lett. **97**, 087207 (2006).

[33] L. Facheris, K. Y. Povarov, S. Nabi, D. Mazzone, J. Lass, B. Roessli, E. Ressouche, Z. Yan, S. Gvasaliya, and A. Zheludev, Spin density wave versus fractional magnetization plateau in a triangular antiferromagnet, Phys. Rev. Lett. **129**, 087201 (2022).

[34] R. Shirakami, H. Ueda, H. O. Jeschke, H. Nakano, S. Kobayashi, A. Matsuo, T. Sakai, N. Katayama, H. Sawa, K. Kindo, C. Michioka, and K. Yoshimura, Two magnetization plateaus in the kagome fluoride Cs$_2$LiTi$_3$F$_{12}$, Phys. Rev. B **100**, 174401 (2019).

[35] Y. Chen, Y. Zhang, R. Li, H. Su, Z. Shan, M. Smidman, and H. Yuan, Multiple magnetic phases and magnetization plateaus in TbRh$_6$Ge$_4$, Phys. Rev. B **107**, 094414 (2023).

[36] Y. Okamoto, D. Nakamura, A. Miyake, S. Takeyama, M. Tokunaga, A. Matsuo, K. Kindo, and Z. Hiroi, Magnetic transitions under ultrahigh magnetic fields of up to 130 T in the breathing pyrochlore antiferromagnet LiInCr$_4$O$_8$, Phys. Rev. B **95**, 134438 (2017).

[37] A. Miyata, H. Ueda, Y. Ueda, H. Sawabe, and S. Takeyama, Magnetic phases of a highly frustrated magnet, ZnCr$_2$O$_4$, up to an ultrahigh magnetic field of 600 T, Phys. Rev. Lett. **107**, 207203 (2011).

[38] Y. H. Matsuda, N. Abe, S. Takeyama, H. Kageyama, P. Corboz, A. Honecker, S. Manmana, G. Foltin, K. Schmidt, and F. Mila, Magnetization of SrCu$_2$(BO$_3$)$_2$ in ultrahigh magnetic fields up to 118 T, Phys. Rev. Lett. **111**, 137204 (2013).